PERGAMON

International Journal of Multiphase Flow 28 (2002) 553–578

International Journal of Multiphase Flow

www.elsevier.com/locate/ijmulflow

Experimental study of bubble injection in a turbulent boundary layer

C. Gabillet, C. Colin, J. Fabre *

Institut de Mécanique des Fluides de Toulouse, UMR CNRS–INP–UPS 5502, Allée du Professeur Camille Soula, F-31400 Toulouse, France

Received 17 May 2000; received in revised form 18 October 2001

Abstract

A bubbly flow experiment has been performed in a horizontal channel in order to simulate the dynamical effects of the nucleation of bubbles and their departure from the wall in boiling flows. Bubbles were injected through a porous plate located on the lower wall. The void fraction, bubble velocity and diameter were measured with a fibre-optic probe and the liquid flow in the bubble layer was studied with a hot film anemometer. The void fraction profiles are nearly self-similar. The expansion of the bubble layer is quasi-linear with the distance downstream, with a rate of expansion depending on the bubble diameter. Comparison with a simple model of bubble trajectories highlights the role of the lift force in the development of the bubble layer. The mean velocity in the bubble layer does not differ greatly from that measured in single-phase flow, except near the wall. The velocity profiles follow a logarithmic law similar to that for turbulent flow over a rough surface suggesting that bubbles attached to the wall act as roughness elements on the liquid flow. The turbulent kinetic energy is greater than in single-phase flow. The additional turbulence is analysed and attributed partly to the relative motion of the bubbles and partly to the augmentation of the turbulent shear stress in the bubble layer.

1. Introduction

Two-phase bubbly flows are present in many practical situations in the thermal, nuclear and chemical industries. Numerical simulation of bubbly flows is often used for the design and the optimisation of industrial devices. The numerical prediction of two-phase bubbly flows requires a careful choice of the boundary conditions on the wall, and the wall region of bubbly flows has therefore been a topic of much interest during the last decade.

* Corresponding author. Tel.: +33-5-6128-5848; fax: +33-5-6128-5891.
E-mail address: fabre@imft.fr (J. Fabre).

0301-9322/02/$ - see front matter
PII: S0301-9322(01)00075-1

It is now well known that wall momentum transfers are deeply linked to the spatial distribution of bubbles. Most of the studies of bubbly flows have been carried out in vertical pipes, with bubbles injected at the inlet section.

In upward vertical bubbly flows in pipes, the bubble drift and the vorticity of the liquid flow induced by the presence of the wall lead to a migration of small bubbles towards the wall (Serizawa et al., 1975; Nakoryakov et al., 1981; Zun, 1988; Liu and Bankoff, 1993). There is a void fraction peak near the wall, with a maximum located at about one bubble diameter from the wall. The presence of bubbles near the wall leads to an increase in the longitudinal liquid velocity with void fraction, due to the effect of buoyancy. The longitudinal velocity profile of the liquid is consequently flatter than in single-phase flow. This is consistent with the observed increase of the wall shear stress (Marié, 1987). Under these conditions, for low liquid velocity and far from the bubble-to-slug transition, the logarithmic wall law for the longitudinal mean velocity of the liquid is still valid (Sato et al., 1981). Moursali et al. (1995) studied a turbulent boundary layer developing on a vertical flat plate in the presence of millimetric bubbles and showed that the slope of the logarithmic law tends to decrease when the peak of void fraction is located in the logarithmic region. This supports the idea of Marié et al. (1997): the change in the slope is closely linked to the void fraction peaking phenomenon. In vertical upward bubbly flows, the void migration towards the wall causes changes in the turbulence structure. In cases of liquid flows at low velocity, the turbulent shear stress near the wall is greater than in single-phase flow and the energy of the fluctuating motion of the liquid is intensified by the relative bubble motion. However, the production of turbulent kinetic energy by the mean velocity gradients and the turbulent shear stress is not really changed in the logarithmic layer (Moursali et al., 1995). For higher liquid velocities, the liquid fluctuating velocity decreases: this is not yet completely understood (Marié, 1987; Herringe and Davis, 1976; Serizawa and Kataoka, 1990).

In vertical downward bubbly pipe flows, a migration of the bubbles towards the pipe axis is observed (Wang, 1985; Nakoryakov et al., 1996). This leads to a decrease of the longitudinal mean velocity of the liquid near the pipe centre. As a consequence, the longitudinal liquid velocity profiles are also flatter than in single-phase flow and the wall shear stress is greater than in single-phase flow. However, the bubbles are almost absent in the near-wall region: the logarithmic law and its slope therefore remain unchanged (Nakoryakov and Kashinski, 1995). The same behaviour of the fluctuating velocities of the liquid is observed in a downward bubbly pipe flow as in an upward flow.

Micro-gravity bubbly flows in pipes have also been studied to analyse the effect of gravity on the void fraction distribution and the flow dynamics (Kamp, 1996). In the liquid phase, neither the mean velocity distribution nor the wall shear stress is modified.

In all these studies, bubbles are injected at the inlet section of the pipe. They may lie close to the wall, as in vertical upward flow, but they are absent from the viscous sub-layer.

In the case of bubble nucleation on the wall, the structure of the liquid flow is expected to change drastically. Moreover, there is in this case a longitudinal evolution of the gas flow rate, which makes the flow more complex to study. Such experiments are somewhat difficult to perform: bubbles may be either injected on the wall or nucleated by the boiling process so that the measurements near the wall are difficult to perform. As a consequence, very few experiments have been reported.

The effect of injection of bubbles at the wall of a horizontal channel has been investigated by Madavan et al. (1984, 1985). The injection of micro-bubbles through a porous plate flush-mounted on the wall leads to a decrease of the wall shear stress. However, the measurements were performed downstream of the injection zone and not above the porous plate, which limits the interpretation of the results.

Velidandla et al. (1995) performed laser Doppler anemometer (LDA) measurements in an upward vertical flow of R113 heated at the internal wall of an annular duct. Their results show that both the logarithmic law and the turbulent kinetic energy profiles are drastically different from those in single-phase flow. However, it is difficult to say whether the wall momentum transfer was modified in their experiment by thermal buoyancy or by bubble drift. By comparison with an isothermal single-phase flow, the wall heat transfer leads to a decrease of the wall shear stress whereas the bubble drift leads to an increase.

To understand the modification of the momentum transfer at the wall by nucleation, growth and bubble departure, an isothermal turbulent water flow in a horizontal rectangular channel, with bubbles injected at the lower wall, is investigated in the present paper. This experiment highlights some of the dynamic effects encountered in boiling flow with high void fraction and sub-millimetric bubbles.

The experimental facility and the operating conditions are presented in Section 2. The measuring techniques – dual fibre-optic probe for the characterisation of the gas phase and hot film anemometer for the investigation of the kinematic structure of the liquid flow – are described in Sections 3 and 4. An overview of the experimental results is given in Section 5. These results are then discussed in Section 6 with a special attention paid to the development of the bubble layer and to the modification of the structure of the mean and turbulent flow in the liquid.

2. Experimental setup and operating conditions

The experimental facility (Fig. 1) consisted of a water loop made of a free surface reservoir, a centrifugal pump, a control valve, a heat exchanger, 25 and 5 μm filters, a diverging–converging section with a honeycomb and a rectangular channel. The horizontal channel was 200 mm wide, 25 mm high and 4 m long. An 8:1 aspect ratio was chosen to obtain a spanwise homogeneous flow. Measurements were performed 1420 mm downstream of the channel's entrance section. In the present experiment, the liquid superficial velocity, j_L, was kept constant and equal to 1.16 m/s. The corresponding Reynolds number Re based on the hydraulic diameter was 51 500.

In order to mimic the dynamic aspects of a boiling flow, air was injected through a porous plate. A sintered Inconel 600 porous plate (class 05) 180 mm wide, 205 mm long and 7 mm thick was flush-mounted at the lower wall of the channel. The volumetric porosity of the plate was between 25% and 30%. The air flow rate was measured by a rotameter and controlled by a manometer. The porous plate started 1390 mm downstream from the inlet. Above the plate, the characteristic of the turbulent liquid flow was checked: the flow was fully developed and homogeneous in the central part of the channel in the spanwise direction. The mean and RMS streamwise velocities of the water flow over the plate were measured with an LDA. They show good agreement with the measurements of Hussain and Reynolds (1975). In particular, they show that, at this Reynolds number, the porous plate behaves as a smooth wall.

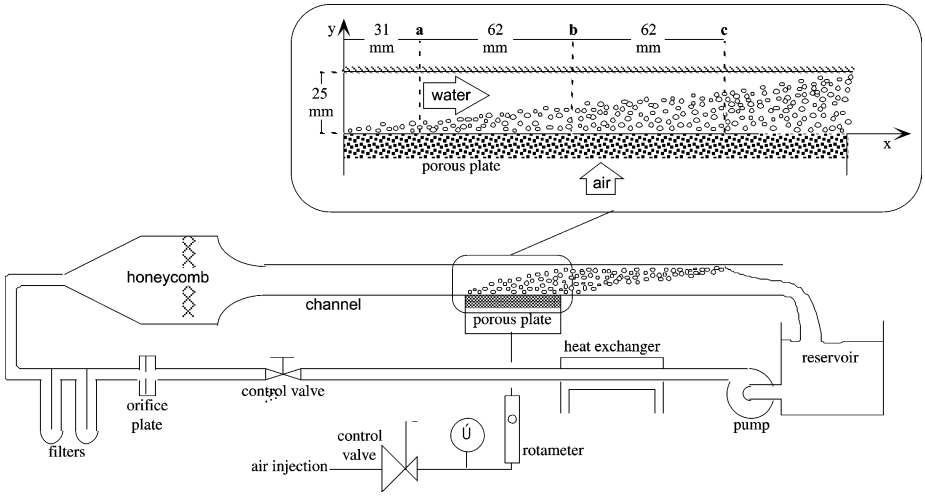

Fig. 1. Experimental setup and location of the measuring test sections.

To investigate the influence of the bubble layer development, two-phase flow measurements were performed in three different cross-sections (a, b and c), located, respectively, at 31, 93 and 155 mm from the upstream edge of the porous plate (Fig. 1). The homogeneity of the air flux was carefully checked in the absence of liquid flow. The air injection was characterised by the volumetric flux j_G across the porous plate, defined as the flow rate per unit surface. The choice of j_G had to satisfy two conflicting conditions:

1. the density of bubbles nucleating at the wall had to be homogeneous;
2. the void fraction had to be moderate, for the liquid velocities to be measured and for the interaction of the bubble layer with the upper wall of the channel to be weak.

j_G has to be high enough to satisfy the first condition, but not too high in order not to violate the second condition. The experiments were carried out with three different air fluxes: 2, 5 and 10 mm/s. When $j_G = 10$ mm/s, the bubble layer reached the top of the channel in the downstream measurement section.

Although the global conditions of air injection (pressure drop across the porous plate, flow rate) were carefully controlled, there is no reason to believe that the injection sites remain the same. However, the repeatability of local void fraction and liquid velocity distributions was checked for all operating conditions and was found acceptable (Gabillet, 1998).

Intrusive probes were introduced into the channel in the different measurement sections through the upper wall. The vertical displacement of the probes was controlled with an accuracy of 10 μm by a micrometer screw. Its position with respect to the porous wall ($y = 0$) was determined in single-phase flow by fitting the mean velocity profile of the liquid by the logarithmic law, the friction velocity u_* being determined from the pressure drop obtained from nine pressure taps along the channel. This adjustment leads to an uncertainty of 0.2 mm for the probe location.

3. Measurement of void fraction, bubble diameter and velocity

3.1. Optical probes

A dual fibre-optic probe was designed especially for this experiment and built by RBI. It consists of two fibres. Each fibre has a diameter of 50 μm and a cone-shaped tip of 15 μm. The distance l_{12} between the two tips is 430 ± 40 μm, comparable to the typical bubble diameter. This choice is a compromise between a good probability to detect a single bubble on the two tips and an acceptable time delay. With this arrangement, the uncertainty in l_{12} leads to a relative uncertainty of $\pm 10\%$ for the bubble velocity measurement. The angle of inclination between the direction of the two tips and the porous plate is smaller than 5° and can be ignored since the induced error resulting from this misalignment is less than 1%. The probe axis is parallel to the mean flow, for a better phase discrimination. The probe is connected to an electronic system (RBI 9110) providing an output voltage signal between 0 and 5 V.

The spatial resolution of the probe is estimated following the results of Cartelier (1990), who measured the response time T_r due to the dewetting of the tip at the passage of a liquid–gas interface for different probes. This response time decreases when the velocity of the interface V_i increases. For each probe, he defined a latency length $L_* = T_r V_i$ that characterises the spatial resolution of the probe, i.e. the minimal bubble diameter below which the bubbles are not correctly detected. For interface velocities greater than 0.3 m/s, L_* is constant. According to the results of Cartellier, the value of L_* for a probe of 15 μm diameter is roughly equal to 150 μm. Thus, the probe used in our experiments is able to detect bubbles greater than 150 μm.

Some bubbles may be deflected due to the obstruction of the probe, and the probe tip was in this case at best only partly dewetted. When the tip pierced the bubble, the amplitude voltage of the output signal was therefore much lower than that measured when the probe was in the gas under static conditions. However, deflection of bubbles at the probe tips occurred mainly for small bubbles, which contributed only weakly to the mean void fraction and to the mean gas velocity.

The sampling frequency, 100 kHz, was sufficiently high so that the velocity uncertainty was smaller than 3%.

Bubbles were detected by using a threshold of the output voltage of the photodetector. This threshold was chosen carefully so that the signal due the passage of small bubbles could be distinguished from noise. The void fraction and each bubble residence time were determined with a relative accuracy of 5% at a distance of 1 mm from the porous wall. The accuracy of the longitudinal mean velocity of the gas was the same.

3.2. Processing techniques for gas velocity and bubble size determination

Whenever the output voltage was greater than the threshold level, the gas characteristic function χ_G was set to 1, otherwise χ_G was set to 0. The local gas void fraction is thus the time average of χ_G. For a double optical probe, the cross-correlation function C of the two characteristic functions $\chi_{G,1}$ and $\chi_{G,2}$ is

$$C = \frac{1}{T} \int_0^{T-\Delta t} \chi_{G,1}(t)\chi_{G,2}(t+\Delta t)\,\mathrm{d}t, \tag{1}$$

where T is the measuring interval. The maximum of C corresponds to a characteristic transit time Δt_p of the bubble between the two probe tips. For a given distance between the two probes l_{12}, a characteristic bubble velocity U_B is obtained:

$$U_B = \frac{l_{12}}{\Delta t_p}. \tag{2}$$

Let us suppose that an interface is detected at the upstream tip and another is detected at the downstream tip at a time Δt later. For the signal processing, a time interval $[t_{min}, t_{max}]$ was chosen. If Δt belongs to $[t_{min}, t_{max}]$, then the two interfaces detected at the two tips are deemed to correspond to the same bubble. A processing method is used to suppress the contribution of two different bubbles found in the range $[t + t_{min}, t + t_{max}]$ (Roig, 1993). The velocity u_B of each bubble is deduced from l_{12} and the bubble transit time Δt. The mean velocity U_G of the gas phase is then calculated from the velocities u_B of n_B bubbles pierced by the two probes, weighted by their residence time t_B over the upstream tip:

$$U_G = \frac{1}{T} \sum_{i=1}^{n_B} t_B(i) u_B(i). \tag{3}$$

The sensitivity of U_G to the choice of the interval $[t_{min}, t_{max}]$ used for data processing was checked by Gabillet (1998) and leads to a relative accuracy of 4%. The gas RMS velocity has not been determined, because it is too sensitive to the choice of the interval and also because the measurement time (80 s) is too small to ensure convergence. Whatever the chosen time interval, the bubble velocity distribution is found to be asymmetric with fewer low velocities. There are two reasons for this:

- bubbles with a low velocity may be deflected and can thereby avoid the downstream probe tip, especially near the wall, where the vertical gas velocity component may be as important as the longitudinal component;
- the bubbles cannot have a velocity smaller than a limit value, even near the wall. Indeed they are put in motion rather quickly. This will be discussed in Section 6.

With the velocity and the residence time of the bubble at the upstream tip, the chord length l_B of the bubble viewed by the tip can be determined:

$$l_B(i) = u_B(i) t_B(i). \tag{4}$$

To calculate the bubble diameter distribution from the measured chord length distribution, the inverse method developed by Clark and Turton (1988) was used. This method enables us to calculate the probability density function of the bubble diameters, if the flow is assumed to be locally homogeneous over a distance greater than the bubble diameter. It requires an assumption on the bubble shape. In our experiment bubbles were sufficiently small so that they could be assumed spherical. This method also requires a great number of samples of the chord length distribution. If the number of samples is too small (especially near the edge of the bubble layer), this inverse method cumulates the errors, leading to negative values of the probability density function of the diameter classes. To avoid this problem, Kamp (1996) assumed that the proba-

bility density function g_0 of the bubble diameters in a turbulent bubbly flow is well fitted by a log-normal law:

$$g_0(d_B) = \frac{1}{\sqrt{2\pi}\sigma d_B} \exp\left[-\frac{(\ln(d_B/d_m))^2}{2\sigma^2} \right], \tag{5}$$

where d_m is the most probable diameter and σ a parameter indicating the width of the distribution. The determination of the probability density function of the bubble diameters is thus reduced to the determination of two parameters d_m, σ. Statistics of the bubble size are then calculated from g_0. They are sensitive not only to the interval $[t_{min}, t_{max}]$ but also to the number of classes of the distribution of the diameters. Therefore the bubble RMS diameter was not calculated. The bubble mean diameter D_B is finally determined with a relative accuracy of 20%.

4. Measurement of liquid velocity

To measure the velocities of the liquid phase, the severe experimental conditions due to the vicinity of the wall and to the high void fraction make the use of LDA inappropriate (Tjiptahardja et al., 1996). Thus a hot film anemometer (HFA) was preferred. Demineralised water was used for these measurements. All the experiments were performed with a superficial velocity of the liquid phase j_L equal to 1.16 m/s, corresponding to a Reynolds number Re of 51 500. In a single-phase flow, when $j_L = 1.16$ m/s, the friction velocity u_* is equal to 0.058 m/s.

4.1. Hot film probes

The system consists of a Dantec Streamline anemometer and a probe with overheat ratio fixed at 0.08. Two different probes were used.

(1) A single boundary layer probe, Dantec 55R15, made of an insulated cylindrical hot wire of 70 μm diameter with a sensitive length of 1.25 mm was chosen to measure the longitudinal mean and RMS velocities. Due to its size, this probe cannot detect the smallest turbulent structures. Indeed the ratio between the probe length and the Kolmogoroff length scale may be significant: 12.5 at the channel axis and 40 at a distance of 1 mm from the porous wall for a superficial liquid velocity $j_L = 1.16$ m/s. Nevertheless, the measurement of the mean longitudinal velocity is not influenced by the probe size. In contrast (Fig. 2), the measurements of the longitudinal RMS velocity $\sqrt{\overline{u_L'^2}}$ display some differences with the measurements performed by LDA and the results of Hussain and Reynolds (1975), for $y^+ = yu_*/\nu < 45$, i.e. $y < 0.75$ mm. The velocity and Reynolds stress components will be scaled by the maximum velocity U_0 at the channel axis, the vertical co-ordinate y, by the half-height of the channel ($h = 12.5$ mm).

(2) A 1249 A–10 W TSI miniature X-array probe made of two insulated cylindrical hot wires of 25 μm diameter with a sensitive length of 0.25 mm was chosen to determine the longitudinal and vertical mean and RMS velocities as well as the turbulent shear stress. The distance between the two wires (0.5 mm) is comparable to the integral turbulent length scale for $y_+ < 75$ ($y/h < 0.1$). Thus, the comparison with the measurements of Laufer (1951) for $Re = 43\,300$ in Fig. 2 shows that the vertical RMS velocity $\sqrt{\overline{v_L'^2}}$ is overestimated for $y/h < 0.1$. Fig. 2 also displays the

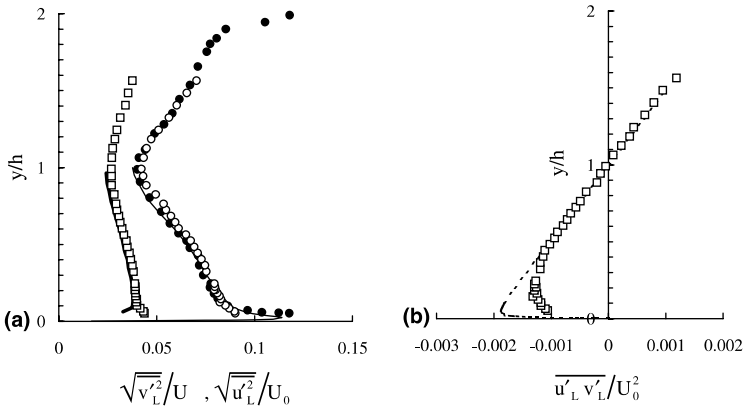

Fig. 2. (a) RMS velocities in single-phase flow for $j_L = 1.16$ m/s: $\sqrt{\overline{u_L'^2}}/U_0$: ● lda, ○ hfa (single probe), _____ Hussain and Reynolds (1975); $\sqrt{\overline{v_L'^2}}/U_0$: □ hfa (dual probe), — Laufer (1951). (b) Turbulent shear stress for $j_L = 1.16$ m/s: □ hfa (dual probe), - - - theory.

dimensionless turbulent shear stress $\overline{u_L' v_L'}/U_0^2$. It is compared to the theoretical turbulent shear stress obtained by subtracting the viscous shear stress from the total shear stress. In a fully developed flow, the total shear stress is linear and equal to $\rho_L u_*^2(1 - y/h)$ and the viscous shear stress is obtained from the mean velocity profile. $\overline{u_L' v_L'}$ is drastically underestimated for $y_+ < 175$, i.e. $y < 3$ mm. In order to improve the determination of the turbulent shear stress near the wall in a two-phase flow, the filtering of the energetic turbulent structures of the liquid is assumed to be the same as in single-phase flow. From the measurements in single-phase flow and the theoretical value of the turbulent shear stress, a filtering correction function is built. This function depends on the distance from the porous wall and is calculated from the ratio of the theoretical value to the measured value. For $y/h > 0.45$, this function is equal to 1; it can reach 1.6 for $y/h = 0.08$.

4.2. Hot film measurement in a two-phase flow

Close to the porous wall, the presence of small bubbles imbedded in highly turbulent liquid makes the discrimination between the phases difficult: a high sampling frequency (20 kHz) and a large time for data acquisition are thus required. To our knowledge, measurements using a hot film anemometer with bubbles of such small diameter have never been performed. Measurements reported in the literature usually concern bubbles 5–10 times larger than in the present experimental study.

During the impact of a bubble on the wire, the HFA output voltage E drops due to the small thermal conductivity of the gas. This voltage drop must not be attributed to the velocity fluctuation and has to be removed from the signal for the calculation of the mean and RMS velocities in the liquid phase. In most previously reported experiments with bubbles a few millimetres in diameters, the double threshold method of Liu and Bankoff (1993) is well adapted for the bubble discrimination. These thresholds are applied on both the output voltage E and its time derivative dE/dt. In the present experiment, since the sensitive part of the wire is longer than the bubbles, it is never completely dewetted during their impact. The voltage drop reaches different levels, which makes the bubble signature difficult to distinguish from the turbulence fluctuations. In order to

Table 1
Relative accuracy for the determination of the different liquid velocity components near the wall

	Single probe (1) (%)	Dual miniature probe (2) (%)
U_L	3	0.2
$\sqrt{\overline{u_L'^2}}$	13	1
V_L		31
$\sqrt{\overline{v_L'^2}}$		1
$\overline{u_L' v_L'}$		32

improve the detection of the small bubbles from the HFA output voltage, the thresholds are preferably applied to E and $(dE^2/dt)^2$ (Gabillet et al., 1998; Gabillet, 1998).

A measurement time of 80 s allows the convergence of the mean and RMS values of the velocity everywhere in the channel. Table 1 contains the relative accuracy of the velocity components for values measured at a distance of 2 mm from the porous wall. The accuracy takes into account the probe calibration and the bubble discrimination on the HFA output signal.

5. Experimental results

5.1. Void fraction

Fig. 3 shows the void fraction profiles in the measurement sections a, b, c, for the different flow conditions: $j_L = 1.16$ m/s and $j_G = 2$, 5 and 10 mm/s. Measurements were started at 1 mm from the wall and continued up to the boundary of the bubble layer.

The vertical distributions of void fraction have some specific features. At about 1.2–1.3 mm from the wall, the void fraction is maximum. Above this point it decreases asymptotically to zero

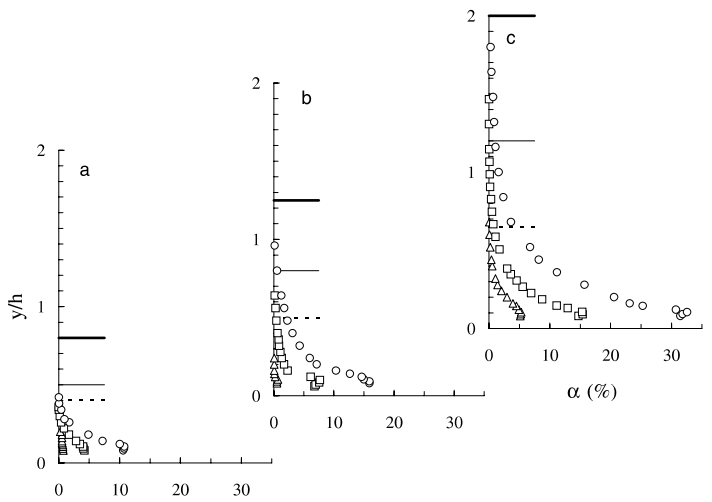

Fig. 3. Void fraction in various measurement sections: △ $j_G = 2$ mm/s, □ $j_G = 5$ mm/s, ○ $j_G = 10$ mm/s; boundary of the bubble layer: - - - $j_G = 2$ mm/s, _____ $j_G = 5$ mm/s, —— $j_G = 10$ mm/s.

at the outer edge of the bubble layer. Below this point, the tendency is not so clear due to the difficulty in getting close to the wall.

As anticipated, the void fraction increases with the air flux near the porous wall. It increases also with the distance x from the upstream edge of the porous plate. The bubble layer develops downstream as would be the case with a thermal layer over a heated plate under the effect of turbulent diffusion and buoyancy. However, in the present case, some additional effects linked to the forces acting on the bubbles are expected.

5.2. Bubble mean diameter

Fig. 4 shows the profiles of the bubble mean diameter D_B for the different flow conditions. As in the case of the void fraction, these profiles suggest the existence of two different sub-layers, an inner layer in the vicinity of the wall where the bubble size grows due to the collision between bubbles leading to coalescence, and an outer layer where the bubble diameter remains almost constant.

In the inner layer, the measurement closest to the wall was performed at 1 mm. Here the bubble diameter is about 0.3 mm for the smallest air flow rate ($j_G = 2$ mm/s). For higher flow rates, the results are not conclusive because of the probable lack of accuracy in a region where the statistical average varies greatly with the distance from the wall. The value of 0.3 mm is in accordance with the bubble diameter at detachment measured by image processing of a high-speed video recording taken at 6000 frames per second at small injection rate. It seems reasonable to believe that the average diameter at bubble departure is close to this value and is almost independent of the global injection rate. When the distance from the wall increases, the bubble diameter increases: the results show that this increase is all the more important as the void fraction is high. This confirms the role of coalescence in the near-wall region where the probability of collision is promoted by both turbulence and bubble density.

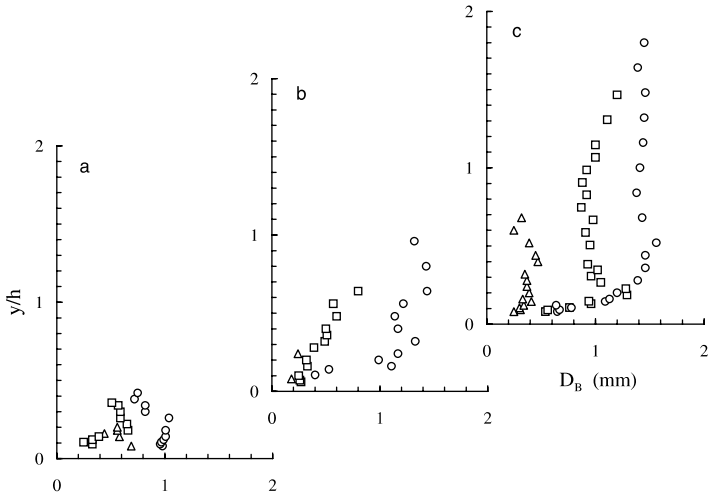

Fig. 4. Bubble mean diameter in various measurement sections: △ $j_G = 2$ mm/s, □ $j_G = 5$ mm/s, ○ $j_G = 10$ mm/s.

In the outer layer the bubble diameter is almost constant. However, it increases with both gas flux and distance from the upstream edge of the porous plate: for example, when $j_G = 10$ mm/s, the mean bubble diameter goes from 1 to 1.3 mm and then to 1.5 mm in sections a, b, c. It is hard to say if coalescence still occurs in the outer layer.

5.3. Mean velocity of the liquid

Velocity measurements were carried out with a single hot film probe, starting from a distance of 0.75 mm from the wall. In single-phase flow, this distance corresponds to $y^+ = 45$. They were also performed with a dual hot film probe for $j_G = 5$ and 10 mm/s in section c starting from a distance of 1 mm from the wall ($y^+ = 60$) in single-phase flow and from a distance of 2 mm in two-phase flow. Velocities are scaled by $U_0 = 1.34 \pm 0.06$ m/s, the maximum value of the mean velocity measured in two-phase flow.

Figs. 5–7 show the profiles of the mean longitudinal velocity U_L measured with the single probe for the three values of j_G. The measurements in single-phase flow are also plotted in these figures. It can be seen that the bubble injection has a very small influence on the mean velocity. Only near the wall is this mean velocity smaller than in single-phase flow. This results from the momentum exchange between phases. Due to this difference, the longitudinal velocity is slightly greater in the central part of the channel. These small modifications have a particular consequence on the wall law, as discussed in Section 6.4.

5.4. Mean velocity of the gas

In the same figures, the velocity profiles of the gas U_G are plotted together with horizontal lines that indicate the limit of the bubble layer δ. The gas moves everywhere slower than the liquid. Near the wall, the gas velocity is smallest and approximately 0.4–0.5 m/s. The velocity difference

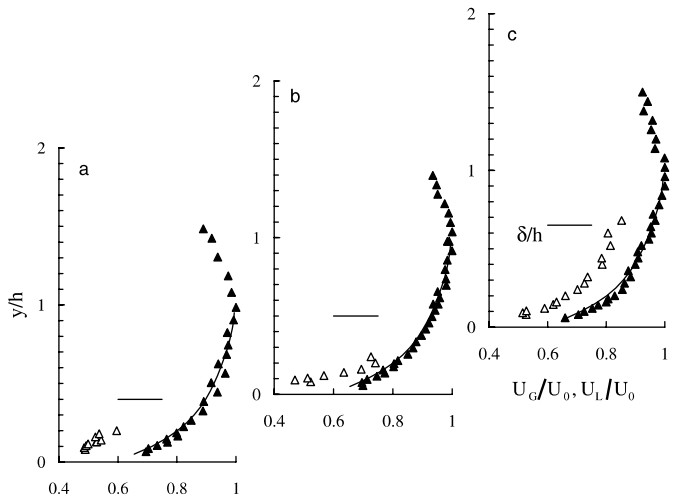

Fig. 5. Mean velocity of liquid and gas in various measurement sections for $j_G = 2$ mm/s: △ U_G/U_0, ▲ U_L/U_0, _____ U_L/U_0 in single-phase flow.

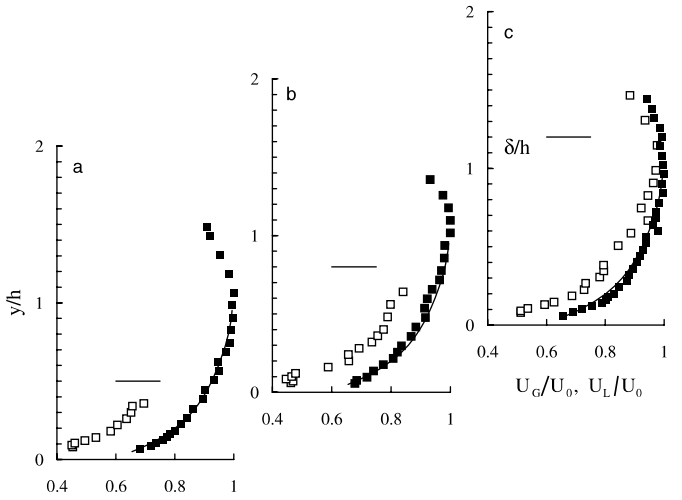

Fig. 6. Mean velocity of liquid and gas in various measurement sections for $j_G = 5$ mm/s: □ U_G/U_0, ■ U_L/U_0, _____ U_L/U_0 in single-phase flow.

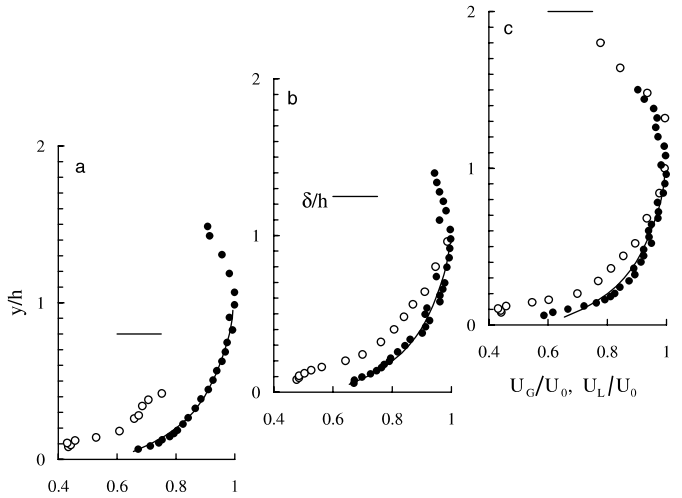

Fig. 7. Mean velocity of liquid and gas in various measurement sections for $j_G = 10$ mm/s: ○ U_G/U_0, ● U_L/U_0, _____ U_L/U_0 in single-phase flow.

$U_L - U_G$ can reach 0.2–0.3 m/s near the wall. When the distance to the wall increases the gas velocity increases. However, the difference of velocities between phases remains significant over the lower part of the bubble layer. The gas reaches the velocity of the liquid only in the axis of the channel for the highest gas flow rate. In the x-direction, the velocity difference $U_L - U_G$ decreases with x. Although surprising it can be explained by the fact that both the local void fraction and the turbulence of the liquid increase with x. Indeed, an increase of the void fraction, in vertical upward flow, tends to diminish the slip velocity, due to hydrodynamics interactions (Kowe et al., 1988). Moreover it has been shown that increase in turbulence tends to decrease the slip velocity in

homogeneous, isotropic turbulence, both in numerical simulations (Spelt and Biesheuvel, 1997) and in experiments (Eppinger, 1995; Poorte, 1998).

5.5. Turbulence of the liquid

Near the wall, since the bubble size is of the same order as the length scale of energy containing eddies (≈ 0.4 mm at 1 mm from the porous plate), the presence of bubbles is expected to modify the turbulence of the liquid phase. The experimental results plotted in Fig. 8 confirm that turbulence is indeed modified within the bubble layer. The RMS velocity $\sqrt{\overline{u_L'^2}}$ is greater than in single-phase flow and increases with void fraction. A similar conclusion can be drawn from the vertical RMS velocity $\sqrt{\overline{v_L'^2}}$ plotted in Fig. 9(a) at section c.

The turbulent shear stress $-\rho_L \overline{u_L' v_L'}$ has also been measured in section c. As in single-phase flow, its determination suffers from a lack of accuracy, due to the filtering effect of the X-array probe. It was necessary to correct its value by using the correction function calibrated in single-phase flow (see Section 4.1). This assumes that the signal filtering is the same as in single-phase flow. This assumption would be correct if the spectral distribution of the turbulence energy was not modified by the presence of bubbles: this is probably not the case. The correction can reach 60% of the measured value for the point closest to the wall, it decreases as the distance from the wall increases: at $y/h = 0.3$, i.e. $y = 4$ mm from the wall, the correction is less than 10%. The corrected results are plotted in Fig. 9(b). For $y/h > 0.4$, the turbulent shear stress remains unchanged in the presence of bubbles. Thus the shear stress is only modified in the lower part of the bubble layer: $|\overline{u_L' v_L'}|$ seems to increase near the wall as the injection rate and the void fraction increase. The different effects responsible for this modification will be analysed in the following section.

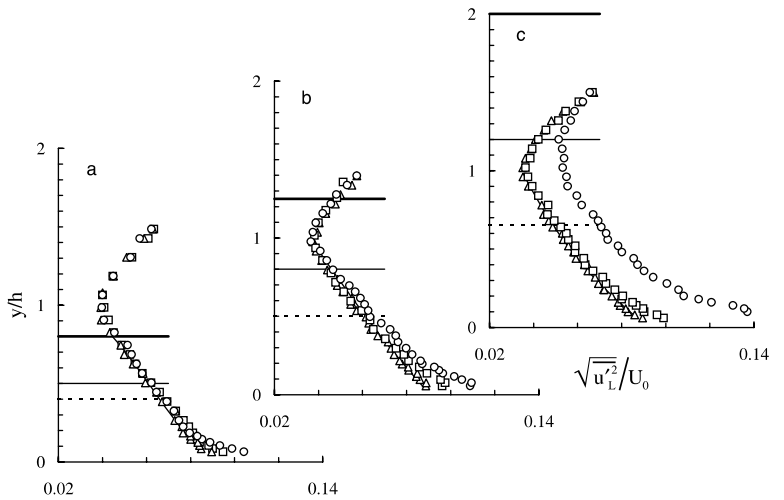

Fig. 8. RMS longitudinal velocity of liquid in various measurement sections: _____ $j_G = 0$ mm/s, △ $j_G = 2$ mm/s, □ $j_G = 5$ mm/s, ○ $j_G = 10$ mm/s; boundary of the bubble layer: - - - $j_G = 2$ mm/s, — $j_G = 5$ mm/s, ——— $j_G = 10$ mm/s.

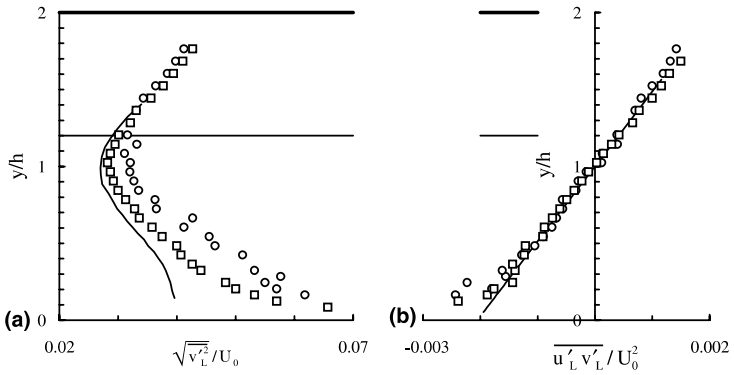

Fig. 9. (a) RMS vertical velocity and (b) turbulent shear stress of liquid in section c: for _____ $j_G = 0$ mm/s, □ $j_G = 5$ mm/s, ○ $j_G = 10$ mm/s; boundary of the bubble layer: — $j_G = 5$ mm/s, ▬ $j_G = 10$ mm/s.

6. Discussion of the results

6.1. Preliminary remark

It was difficult experimentally to ensure a uniform gas flux throughout the porous wall. Even if the homogeneity was checked with air alone, there is no guarantee of homogeneity when water flows over the wall because capillary forces may prevent the gas from flowing through certain pores. For each flow condition, the experimental results on gas velocity and void fraction are used to check whether the air flux through the porous plate is the same between two consecutive measurement sections. Using mass conservation between the sections located at x_1 and x_2 and assuming that the flow is homogeneous in the spanwise direction, we obtain

$$\left[\int_0^{2h} \alpha U_G \, dy\right]_{x_1}^{x_2} = \int_{x_1}^{x_2} j_G \, dx. \tag{6}$$

The above equation expresses the fact that the air flow rate flowing in the channel between sections x_1 and x_2 equals the flow rate injected through the plate in-between. The results are given in Table 2. However, only between sections b and c was the homogeneity acceptable: the porous plate did not properly inject air bubbles between sections a and b. This remark must be kept in mind in the discussion of the results.

6.2. Development of the bubble layer

The bubble layer thickness has been characterised by superimposing the void fraction profiles according to the following equation:

Table 2
Homogeneity of the air injection between sections b and c

j_G (mm/s)	2	5	10
q_G (mm^3/s) calculated from the RHS of Eq. (6)	124	310	620
q_G (mm^3/s) determined from the LHS of Eq. (6)	115	246	634

$$\alpha = \alpha_0 f\left(\frac{y}{\delta}\right), \tag{7}$$

where δ is a bubble layer thickness and α_0 a characteristic void fraction near the porous plate that depends on x and j_G. They can be determined with a relative accuracy of $\pm 14\%$ and $\pm 20\%$, respectively. The results are plotted in Fig. 10(a). They are well grouped for sections b and c and for $j_G = 5$ and 10 mm/s.

It must be pointed out that Eq. (7) expresses the self-similarity of the void fraction evolution. However, for α to be self-similar, all the kinematic variables must be self-similar too. Obviously, U_L does not fulfil this condition so there is no reason why α should be self-similar. The method was only used to determine the bubble layer thickness with an objective criterion.

The evolution of the bubble layer thickness δ with respect to the longitudinal distance x is plotted in Fig. 10(b). It is interesting that δ expands almost linearly with x, both thickness and rate of expansion increasing with the air flux.

To understand the development of the bubble layer it is necessary to underscore the specific role of each force acting on the bubbles. Let us consider a simple model in which the influence of both turbulence and interaction between bubbles is ignored. The role of turbulence will be discussed later. As the void fraction is weak almost everywhere, the neglect of bubble interactions is acceptable. The experimental results show that the liquid flow can be considered fully developed. For simplicity the bubble diameter is assumed constant. Within this framework, the equation of the motion of an isolated spherical bubble of diameter d_B and velocity $\boldsymbol{u}_B$ is expressed by

$$C_D \frac{\pi d_B^2}{4}\rho_L \frac{(\boldsymbol{u}_L - \boldsymbol{u}_B)|\boldsymbol{u}_L - \boldsymbol{u}_B|}{2} + \frac{\pi d_B^3}{6}\rho_L \left\{ C_L(\boldsymbol{u}_L - \boldsymbol{u}_B) \wedge \boldsymbol{\Omega}_L - C_A \frac{\mathrm{d}\boldsymbol{u}_B}{\mathrm{d}t} - \boldsymbol{g} \right\} = \boldsymbol{0}, \tag{8}$$

where $\boldsymbol{u}_L$ and $\boldsymbol{\Omega}_L$ are the velocity and vorticity of the liquid. As $\rho_G \ll \rho_L$, the bubble inertia is neglected. The LHS is the sum of the drag, lift, added mass and buoyancy forces. Unfortunately, the values of the lift and drag coefficients are unknown for spherical bubbles moving near a wall. These coefficients are thus taken equal to their value in an unbounded medium. The lift and added

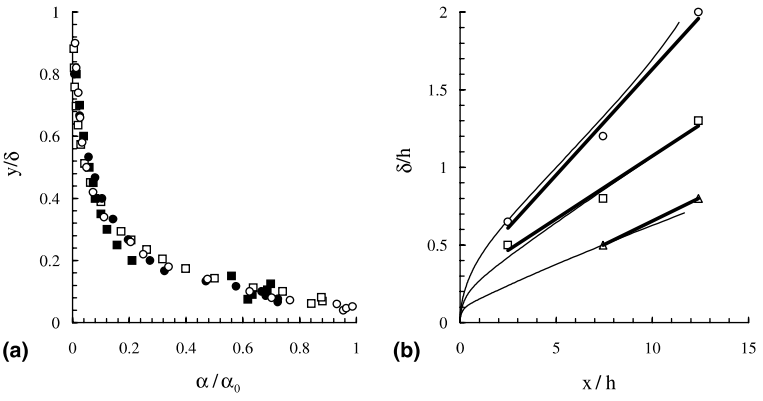

Fig. 10. (a) Self-similarity of void fraction: section b: ■ $j_G = 5$ mm/s, ● $j_G = 10$ mm/s; section c: □ $j_G = 5$ mm/s, ○ $j_G = 10$ mm/s. (b) Evolution of bubble layer thickness: △ $j_G = 2$ mm/s, □ $j_G = 5$ mm/s, ○ $j_G = 10$ mm/s, — linear best fit, _____ numerical predictions of Eqs. (12) and (13).

mass coefficients C_L and C_A are kept equal to their standard value of 0.5, appropriate for the range of bubble Reynolds numbers in our experiment ($Re_B = |\boldsymbol{u}_L - \boldsymbol{u}_B| d_B/\nu_L \approx 50$–$200$). The drag coefficient is written for convenience in the form $C_D = k/Re_B$, where k is itself a function of Re_B. For the values of Re_B under consideration, the terminal velocity correlation of Peebles and Garber (1953) was used for the determination of C_D, because it agrees with experimental results for tap water (Maxworthy et al., 1996). With an adjustment to get a fractional power of the Reynolds number, it can be expressed as $C_D = 17Re_B^{-2/3}$. Finally the longitudinal and vertical components of the momentum equation can be written as follows:

$$C_A \frac{du_B}{dt} = \frac{3k}{4} \frac{\nu_L}{d_B^2}(U_L - u_B) + C_L v_B \frac{dU_L}{dy}, \tag{9}$$

$$C_A \frac{dv_B}{dt} = -\frac{3k}{4} \frac{\nu_L}{d_B^2} v_B + g + C_L (U_L - u_B) \frac{dU_L}{dy}. \tag{10}$$

They show the role of the different forces acting on the bubbles. At the start of its trajectory, the bubble is in the high vorticity region near the wall. As the bubble separates from the wall, the horizontal component of its velocity, u_B, increases because of the drag exerted by the liquid (Eq. (9)). As soon as the vertical velocity component becomes significant, the lift force reinforces the drag effect to reduce the velocity difference $u_B - U_L$ between gas and liquid. As $U_L - u_B$ is positive, the vertical component of the lift force is positive too: it has the same effect as buoyancy to increase the vertical velocity (Eq. (10)). Later, far from the wall, the velocity gradient decreases and so does the lift force: both drag and buoyancy become dominant. The bubble velocity reaches an asymptotic value: its horizontal component tends to U_L and its vertical component, to the terminal velocity v_∞:

$$v_\infty = 0.15 g^{3/4} d_B^{5/4} \nu_L^{-1/2}, \tag{11}$$

that results from a balance between drag and buoyancy. Keeping in mind that U_L depends only on y, then u_B and v_B are invariant under longitudinal translation.

Thus we now consider the y-distribution of the velocity components. Eqs. (9) and (10) are put in dimensionless form by scaling the horizontal velocities by the maximum liquid velocity in the single-phase flow U_0, the vertical velocity by the terminal bubble velocity v_∞ and the vertical co-ordinate by the half-height h of the channel. Since $v_B\,dt = dy$, the time can be replaced by the vertical co-ordinate and Eqs. (9) and (10) become

$$Fr_B \tilde{v}_B \frac{d}{d\tilde{y}}(\tilde{U}_L - \tilde{u}_B) = -2(\tilde{U}_L - \tilde{u}_B), \tag{12}$$

$$Fr_B \tilde{v}_B \frac{d}{d\tilde{y}} \tilde{v}_B = 2(1 - \tilde{v}_B) + N(\tilde{U}_L - \tilde{u}_B) \frac{1}{\kappa \tilde{y}}, \tag{13}$$

where the added mass and lift coefficients are replaced by their numerical values and the liquid velocity is expressed by the logarithmic defect law $U_L = U_0 + (u_*/\kappa)\ln(y/h)$, in which $\kappa = 0.41$ is the von Karman constant. The governing equations of the bubble motion reduce to a set of differential equations whose solution gives the relative bubble velocity. This relative motion is controlled by two dimensionless numbers: $N = U_0 u_*/gh$ which is similar to a Froude number and $Fr_B = v_\infty^2/gh$ which is a Froude number associated with the terminal bubble velocity. In our ex-

periment, $N = 0.8$. In contrast Fr_B takes different values for the various flow conditions because v_∞ changes with the bubble diameter. This suggests that coalescence in the near-wall region plays a dominant role in the development of the bubble layer.

To get a qualitative idea of the bubble motion, the bubble velocity is determined from a numerical solution of Eqs. (12) and (13) for different values of Fr_B, with the initial condition $\boldsymbol{u}_B = \mathbf{0}$ at bubble departure, i.e. at $y = d_B/2$. The results make it possible to identify the region in which the bubble has reached its asymptotic behaviour ($u_B = U_L$, $v_B = v_\infty$). The evolution of the thickness Δ of this region is plotted in Fig. 11(a). It turns out that the dimensionless thickness Δ/h grows linearly with the bubble Froude number Fr_B. The distribution of velocity components is plotted in Fig. 11(b) versus y/Δ for two extreme values of Fr_B corresponding to $d_B = 0.5$ and 1.15 mm: $u_B - U_L$ appears to be nearly independent of Fr_B whereas $v_B - v_\infty$ is more sensitive to the initial conditions that are taken at $y = d_B/2$. The bubbles reach $y = \Delta$ very quickly and, for each case under investigation, before they reach the channel axis. The vertical velocity increases with the distance and reaches a maximum located around $y/\Delta = 0.2$. The maximum velocity $v_{B,max}$ can be two to five times as high as the terminal velocity v_∞ depending on the bubble size. This effect is due to the efficiency of the lift force to increase the vertical bubble velocity. For y/Δ greater than 0.2, the vertical velocity decreases. The horizontal component of the relative velocity decreases monotonously with the distance. When the bubble reaches the limit of the layer $y = \Delta$, $u_B = U_L$ and $v_B = v_\infty$ and the trajectory becomes almost linear since U_L is nearly constant. The layer of thickness Δ will be referred to as the "inertia-dominated" region since the added mass and lift forces play a significant role. It spreads out as the square of the terminal velocity. Outside this layer, the bubble moves in the "drag-dominated" region.

The model can be used to understand the development of the bubble layer. If turbulent dispersion is ignored the bubbles at the bubble layer boundary are those which are issued from the upstream edge of the porous plate. It is possible to determine the trajectory of these bubbles starting from their initial position at ($x = 0$, $y = d_B/2$). For each flow condition, a value of d_B can be chosen so that the bubble trajectory best fits the bubble layer boundary. The selected values are in the range of the measured mean diameters (see Table 3), in particular for the most reliable

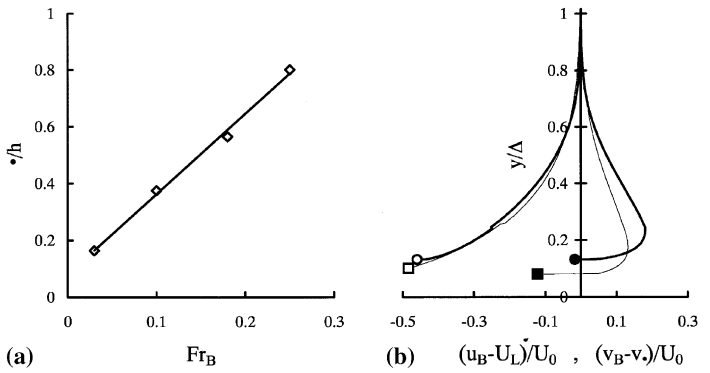

Fig. 11. (a) Development of the inertia-dominated layer. (b) Longitudinal and vertical bubble velocity as calculated from Eqs. (12) and (13): $(u_B - U_L)/U_0$ for: –□– $Fr_B = 0.25$, –○– $Fr_B = 0.03$; $(v_B - v_\infty)/U_0$ for: –■– $Fr_B = 0.25$, –●– $Fr_B = 0.03$.

Table 3
Characteristics of the bubbles moving at the bubble layer edge

	$j_G = 2$ mm/s	$j_G = 5$ mm/s	$j_G = 10$ mm/s
D_B (mm) from experiments	0.3–0.5	0.6–1.1	1–1.5
d_B (mm) used in the model (Eqs. (9) and (10))	0.50	0.80	1.15
v_∞ (cm/s) from Eq. (11)	6.1	11.0	17.4
Δ (mm) from the model (Eqs. (9) and (10))	2.05	4.7	10

results of $j_G = 10$ mm/s. The trajectories are superimposed in Fig. 10(b). For each flow condition one specific trajectory is plotted. At departure, the bubble moves almost vertically due to the strong effect of the y-component of the lift force. In the "inertia-dominated" region, the bubble trajectory curves downstream and becomes almost linear and asymptotic to the bubble boundary in the "drag-dominated" region.

The linear behaviour of the bubble layer thickness is thus linked to the trajectory of the bubbles in the "drag-dominated region". Indeed the mass balance equation for steady flow,

$$\alpha \operatorname{div} \boldsymbol{u}_G + \boldsymbol{u}_G \cdot \mathbf{grad}\,\alpha = 0, \tag{14}$$

shows that, close to the bubble boundary, $\boldsymbol{u}_G$ and $\mathbf{grad}\,\alpha$ are orthogonal, since the first term vanishes with α. Thus the bubble layer boundary is also a streamline of the mean gas flow. As suggested by the result of Fig. 10(b), $\boldsymbol{u}_G$ has a fixed direction for each flow condition. In the "drag-dominated" region, v_B/u_B is nearly constant for a bubble of given diameter since $v_B = v_\infty$ and $u_B = U_L \approx U_0$. By using Eq. (11), it can be seen that the bubble layer develops as

$$\frac{\mathrm{d}\delta}{\mathrm{d}x} = 0.15 \frac{g^{3/4} d_B^{5/4}}{v_L^{1/2} U_L}, \tag{15}$$

in the "drag-dominated region", i.e. if $\delta > \Delta$. This reveals the sensitivity of the development of the bubble layer to the flow conditions and to the bubble diameter. It is rather surprising that δ does not depend on the gas flux j_G. However, it must be kept in mind that the bubble diameter at departure depends on j_G so that the bubble layer indirectly depends on the gas flux.

Let us now discuss the influence of the turbulence on the bubble motion at the boundary of the bubble layer. To analyse the capture of the bubbles by the turbulent eddies, three time scales must be considered (Spelt and Biesheuvel, 1997):

- the response time of the bubbles $t_r = 2d_B^2/3kC_M v_L$ (with $k = C_d Re_B$),
- the characteristic time scale of the largest eddies $t_e = l_e/u'_L$,
- the interaction time of a bubble with a large eddy $t_i = l_e/v_\infty 2g$ (v_∞ being the bubble terminal velocity).

In our case an additional time scale can be defined: the time required for a bubble to reach the boundary of the bubble layer $t_\delta = \delta/v_\infty$.

For bubbles with a diameter of about 0.8 mm, $t_r \approx 10$ ms, $t_e \approx 60$ ms, $t_i \approx 30$ ms and $t_\delta < 10$ ms. The response time t_r is shorter then the time scale t_e of the largest eddies, but longer then the interaction time t_i of the bubble with the turbulent structures. Furthermore the time for the

bubbles to reach the bubble layer boundary is very short $t_\delta < 10$ ms, and the turbulence is not expected to affect the bubble trajectories at these short time scales.

6.3. Modification of the wall shear stress

Before discussing how the bubble motion modifies the mean velocity and the turbulent kinetic energy, it is necessary to understand the mechanism that controls the modification of the shear stress in the bubble layer and at the wall. Let τ^t be the total shear stress defined as the sum of the viscous and the turbulent shear stresses:

$$\tau^t = \rho_L \left(\nu_L \frac{dU_L}{dy} - \overline{u'_L v'_L} \right). \tag{16}$$

Except in the viscous sub-layer, the total shear stress is dominated by the turbulent shear stress. It is shown in Fig. 9(b) that τ^t increases in the bubble layer near the wall. However, the measured values of $\overline{u'_L v'_L}$ is uncertain due to the filtering effect of the probe in the near-wall region. Therefore, the validity of the measured distribution has to be confirmed. This was done theoretically from the mixture momentum equation in which τ^t appears beside other terms containing velocity and pressure. Since the bubble layer behaves as a boundary layer, an asymptotic method can be used to simplify the momentum equation. The details of the assumptions and analytical development are given in the Appendix A. It is shown that the shear stress $\tau^t(x, y)$ in the liquid phase is deduced from the following approximate momentum balance:

$$(1-\alpha)\tau^t - \tau_0^t \approx \rho_L g \int_\delta^y \frac{\partial}{\partial x} \left[\int_\delta^y \alpha \, dy \right] dy. \tag{17}$$

Here, $\tau_0^t(x, y)$ is the shear stress that would exist in a single-phase flow of identical pressure gradient. Eq. (17) shows that the modification of the shear stress is mainly due to buoyancy. Indeed, as inertia has only a marginal effect, the x-momentum balance reduces to a competition between the wall friction and the pressure difference in the x-direction. It may be easily understood that the pressure difference is greater in two-phase flow. Indeed, if the pressure gradient is the same as in single-phase flow at the upper wall, it becomes greater at the lower wall because the presence of bubbles reduces the pressure difference between the upper and lower walls. To compensate for this additional pressure difference, the wall shear stress at the lower wall has to be greater.

Eq. (17) may be simplified by assuming that the void fraction follows the self-similar distribution given by Eq. (7). It yields

$$(1-\alpha)\tau^t - \tau_0^t \approx \rho_L g \delta \frac{d}{dx}(\alpha_0 \delta) \int_\eta^1 \int_\xi^1 f(\zeta) \, d\zeta \, d\xi, \tag{18}$$

where τ^t is a function of both x and $\eta = y/\delta$. Eq. (18) is compared to the experimental results in Fig. 12(a). It gives a good estimate of the y-distribution of τ^t although there is a tendency to slightly overestimate its values. With this theory, the wall shear stress increases when bubbles are injected at the wall and thus the friction velocity can be expressed as

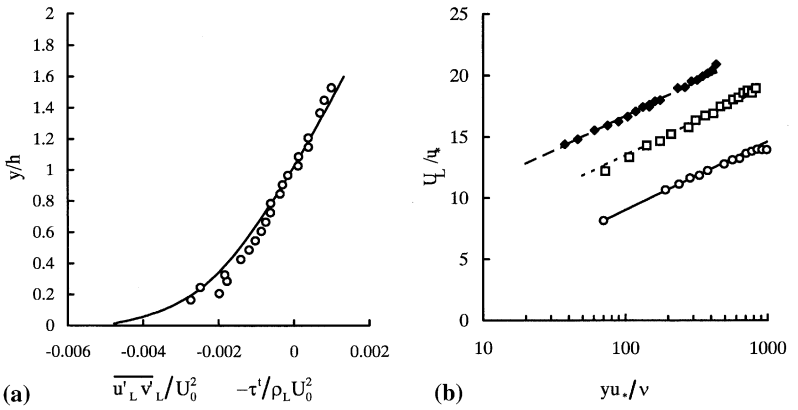

Fig. 12. (a) Shear stress for $j_G = 10$ mm/s in section c: ○ turbulent shear stress, _____ total shear stress deduced from Eq. (18). (b) Logarithmic laws for the liquid velocity in section c: ◆ $j_G = 0$ mm/s, □ $j_G = 5$ mm/s, ○ $j_G = 10$ mm/s, Eq. (20) with: _____ $u_* = 0.058$ mm/s and $B = 5$, - - - $u_* = 0.069$ mm/s and $B = 2.3$, – – – $u_* = 0.094$ mm/s and $B = -2.2$.

$$u_* \approx \sqrt{\frac{1}{1-\alpha_0}\left[u_{*0}^2 + g\delta\frac{\mathrm{d}}{\mathrm{d}x}(\alpha_0\delta)\int_0^1\int_0^1 f(\zeta)\,\mathrm{d}\zeta\,\mathrm{d}\xi\right]}. \tag{19}$$

6.4. Modification of the logarithmic law

As mentioned before, the mean velocity in two-phase flow is nearly the same as in single-phase flow. Therefore, it is relevant to check the validity of the logarithmic law. With the values of the friction velocity experimentally determined and reported in Table 4 for each flow condition, the dimensionless velocity profile $U_{L+} = U_L/u_*$ has been plotted in Fig. 12(b) versus $y_+ = yu_*/\nu$. The log-law

$$U_{L+} = \frac{1}{\kappa}\ln(y_+) + B \tag{20}$$

remains clearly valid in a two-phase flow with the same value of the von Karman constant κ. Its validity suggests that the equilibrium between production and dissipation rates of turbulence persists even in the presence of bubbles in the buffer layer.

Table 4
Friction velocity and logarithmic law coefficients

Section c	$j_G = 0$ mm/s	$j_G = 5$ mm/s	$j_G = 10$ mm/s
Liquid flux, j_L (m/s)	1.16	1.16	1.16
Cross-sectional averaged void fraction (%)	0	1.9	5.4
Friction velocity, u_* (m/s)	0.058	0.069	0.094
Constant B in the log-law	5	2.3	−2.2
Roughness Reynolds no. k, Re_k (see Eq. 21)		26	80
Apparent roughness, k_B (mm)		0.37	0.86

Nevertheless, the constant B decreases with increasing gas flux as shown in Table 4. A similar behaviour is observed in single-phase flow over a rough surface: when the roughness increases the constant B decreases and is given as a function of the roughness height k_B by (Ligrani and Moffat, 1986)

$$B = 8.5 - \frac{1}{\kappa}\ln(Re_k) \quad \text{for } Re_k = \frac{k_B u_*}{\nu} > 55, \tag{21}$$

$$B = 5 + \left[3.5 - \frac{1}{\kappa}\ln(Re_k)\right]\sin\left[\frac{\pi}{2}\frac{\ln(Re_k/15)}{\ln(55/15)}\right] \quad \text{for } 11 < Re_k < 55. \tag{22}$$

As the bubble diameter increases with the gas flux, this suggests that the bubbles, before they detach from the wall, are viewed by the liquid flow as roughness elements. An equivalent bubble roughness k_B can be estimated for each flow condition by using the experimental value of the additive constant B. Eq. (22) is used for $j_G = 5$ mm/s, whereas Eq. (21) is used for $j_G = 10$ mm/s. The results are given in Table 4. The calculated values are, broadly speaking, in accordance with the measured bubble diameter near the wall.

In upward bubbly flow, the modification of the constant B was also demonstrated by Moursali et al. (1995). In contrast to the present study, they noted that B increases with the void fraction as the consequence of the increase of the velocity in the logarithmic region. Indeed, there is no reason to expect the same behaviour when bubbles are injected at the pipe inlet of a vertical flow.

6.5. Additional turbulence

The results of Figs. 8 and 9(a) show that the turbulence intensity is greater than in single-phase flow wherever the bubbles are present. This additional turbulent kinetic energy (TKE) is strictly limited to the bubble layer. It may originate either from a modification of the turbulence production by the work of stress against the strain rate or from the relative motion of bubbles.

The first conjecture can be checked by plotting the turbulence production in the liquid. In our experiment, the gradients with respect to x are negligible so that the turbulence production per unit mass, Π_L, may be expressed by

$$\Pi_L = -\overline{u'_L v'_L}\frac{\partial U_L}{\partial y}. \tag{23}$$

By using the experimental values of both liquid velocity and turbulent shear stress, Π_L may be calculated. Its y-distribution is plotted in Fig. 13(a) for both single-phase and two-phase flow and compared to the theoretical profile deduced from the logarithmic law:

$$\Pi_L = \frac{u_*^3}{\kappa y}\left(1 - \frac{y}{h}\right). \tag{24}$$

As a result one observes that the turbulence production is slightly greater in two-phase flow, but this is insufficient to explain the additional turbulence, observed in Figs. 8 and 9.

To check the second conjecture, we determined the excess of the longitudinal and vertical contributions of the TKE, $\overline{u'^2_b} = \overline{u'^2_L} - \overline{u'^2_{L0}}$ and $\overline{v'^2_b} = \overline{v'^2_L} - \overline{v'^2_{L0}}$, where $\overline{u'^2_{L0}}$ and $\overline{v'^2_{L0}}$ are the corresponding values in single-phase flow. They are plotted in Fig. 13(b) versus the void fraction α. It can be seen that both $\overline{u'^2_b}$ and $\overline{v'^2_b}$ are proportional to α whatever the gas flux and the distance from

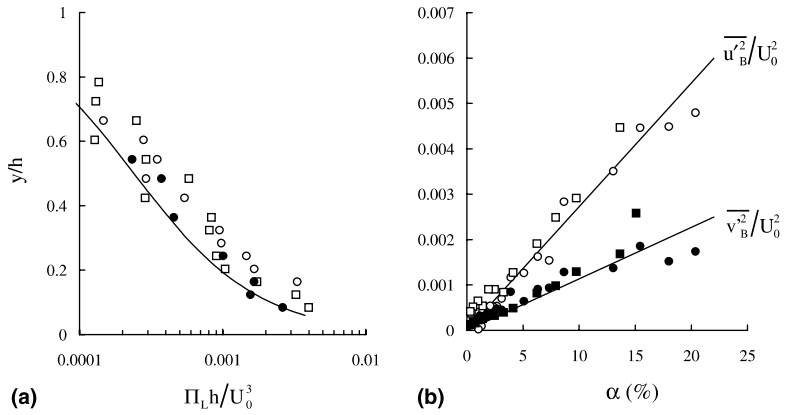

Fig. 13. (a) Production of turbulent kinetic energy in section c for ● $j_G = 0$ mm/s, □ $j_G = 5$ mm/s, ○ $j_G = 10$ mm/s, _____ Eq. (24). (b) Additional contributions to the turbulent kinetic energy in section c: $\overline{u'^2_B}/U_0^2$ for □ $j_G = 5$ mm/s, ○ $j_G = 10$ mm/s; $\overline{v'^2_B}/U_0^2$ for ■ $j_G = 5$ mm/s, ● $j_G = 10$ mm/s.

the wall. Last but not least, the excess of energy is not isotropic. The x-contribution to the turbulence energy $\overline{u'^2_b}$ is nearly twice as great as $\overline{v'^2_b}$. This is certainly due to the fact that this additional turbulence is mainly controlled by the drift velocity of bubbles which is nearly parallel to the wall. In fact, near the wall $\overline{v'^2_b}/\overline{u'^2_b}$ is constant and roughly equal to 0.4, smaller than the ratio 0.75 obtained for bubble-induced turbulence in potential flow theory (Biesheuvel and van Wijngaarden, 1984), but closer to the value for the shear-induced turbulence. Nevertheless, the present results suggest that the additional turbulence is produced by both bubble relative motion and shear-induced turbulence. [1] The process of injection at the wall does not contribute to any discernible effect.

7. Conclusion

An experiment simulating the dynamic effect of convective boiling in a horizontal channel has been performed. Bubble nucleation was simulated by gas injection through a porous plate located on the lower wall. Small air bubbles of the same size as vapour bubbles encountered in subcooled boiling were generated. They formed a bubble layer that developed in the liquid flow. The structure of this layer has been characterised by measuring both velocity and turbulence of the liquid with hot film probes, and by measuring void fraction, gas velocity and bubble diameter

[1] However, an additional turbulence is also observed for $j_G = 10$ mm/s near the channel axis in section c, in a region where the void fraction and the bubble drift velocity are low. For all the runs, other than this, the bubble-induced turbulence is produced in the near-wall region, where a local equilibrium exists between production and dissipation and where the turbulence diffusion does not affect the balance. For $j_G = 10$ mm/s, in section c, the local void fraction and the slip velocity are significant outside the near-wall region, and this additional turbulence is expected to diffuse toward the axis where it accumulates. This mechanism could explain the additional turbulence observed near the channel axis for $j_G = 10$ mm/s in Figs. 8 and 9.

with optical probes. This is an interesting example of developing flow in which the lift force plays a specific role: it reinforces the role of buoyancy in moving the bubbles away from the lower wall.

The first noticeable result concerns the bubble layer. Its linear expansion is found experimentally and reproduced theoretically with a simple model that reveals the existence of two regions: a near-wall "inertia-dominated" region in which both lift force and coalescence play a dominant role and a "drag-dominated" region where bubbles have already been put in motion by the liquid. This model also shows that the expansion rate essentially depends on the bubble diameter. The quasi-self-similarity of the void fraction profile is also observed experimentally.

The second result concerns the modification of the liquid velocity and turbulence by the bubble injection. The mean velocity is nearly the same as in single-phase flow, except near the wall where the shear stress is greater than in single-phase flow. The log-law remains valid and the liquid flow behaves as over a rough surface. It is seen that the calculated roughness deduced from the velocity profile is correlated to the bubble diameter at departure from the wall. Another difference with single-phase flow lies in the turbulent kinetic energy. An additional turbulent energy, almost linearly correlated with the void fraction, has been highlighted. It appears to be strongly anisotropic. It results from two combining effects: bubble-induced turbulence and shear-induced turbulence.

Acknowledgements

The authors would like to than EDF (Direction des Etudes et Recherches) for funding this research project.

Appendix A

The determination of the evolution of the turbulent shear stress starts from the momentum balance of the gas–liquid mixture. By neglecting the mean and turbulent contributions of the gas inertia and the viscous stresses and by assuming that the phase averaged pressure is the same in both phases, the two projections of this equation read

$$(1-\alpha)\underbrace{\left[U_{\mathrm{L}}\frac{\partial U_{\mathrm{L}}}{\partial x}+V_{\mathrm{L}}\frac{\partial U_{\mathrm{L}}}{\partial y}\right]}_{(\varepsilon)}=-\underbrace{\frac{1}{\rho_{\mathrm{L}}}\frac{\partial P}{\partial x}}_{(1)}-\underbrace{\frac{\partial}{\partial x}\left[(1-\alpha)\overline{u_{\mathrm{L}}'^{2}}\right]}_{(\varepsilon)}-\underbrace{\frac{\partial}{\partial y}\left[(1-\alpha)\overline{u_{\mathrm{L}}'v_{\mathrm{L}}'}\right]}_{(1)},$$

$$(1-\alpha)\underbrace{\left[U_{\mathrm{L}}\frac{\partial V_{\mathrm{L}}}{\partial x}+V_{\mathrm{L}}\frac{\partial V_{\mathrm{L}}}{\partial y}\right]}_{(\varepsilon^{3})}=-\underbrace{\frac{1}{\rho_{\mathrm{L}}}\frac{\partial P}{\partial y}}_{(1)}-\underbrace{\frac{\partial}{\partial x}\left[(1-\alpha)\overline{u_{\mathrm{L}}'v_{\mathrm{L}}'}\right]}_{(\varepsilon^{2})}-\underbrace{\frac{\partial}{\partial y}\left[(1-\alpha)\overline{v_{\mathrm{L}}'^{2}}\right]}_{(\varepsilon)}-\underbrace{(1-\alpha)g}_{(\varepsilon)}. \quad \text{(A.1)}$$

The development of the bubble layer is similar to the development of a 2D boundary layer. Thus the small parameter ε that compares the velocity gradients in the longitudinal and in the vertical directions can be introduced. By considering the continuity equation, the boundary layer assumption implies that the liquid flow is quasi-parallel. This assumption has been verified

experimentally. The mean and RMS velocities, the pressure and both longitudinal and vertical coordinates are scaled as follows:

$$U_L = U_0\tilde{U}_L, \quad V_L = \varepsilon U_0\tilde{V}_L, \quad \overline{u_L'^2} = u_*^2\overline{\tilde{u}_L'^2}, \quad \overline{v_L'^2} = u_*^2\overline{\tilde{v}_L'^2}, \quad P = \rho_L U_0^2\frac{\tilde{P}}{\varepsilon}, \quad x = \frac{\delta\tilde{x}}{\varepsilon},$$
$$y = \delta\eta, \quad \varepsilon = \frac{\mathrm{d}\delta}{\mathrm{d}x}, \tag{A.2}$$

where dimensionless quantities are denoted by $\sim$. By using these quantities, Eqs. (A.1) can be written in dimensionless form. Thus the order of the different terms of the momentum balance can be determined as shown in Eqs. (A.1).

At order ε, the integration of the second of Eqs. (A.1) along the vertical axis gives the vertical pressure distribution

$$P = P(\delta) + \left[\rho_L\overline{v_L'^2}\right]_{y=\delta} - \rho_L(1-\alpha)\overline{v_L'^2} - \int_\delta^y \rho_L(1-\alpha)g\,\mathrm{d}y. \tag{A.3}$$

At the upper boundary of the bubble layer, the mean and RMS velocity components and the longitudinal pressure gradient remain the same as in single-phase flow. By using Eq. (A.3), the momentum balance in the longitudinal direction can be integrated along y. At order ε, the shear stress τ^t is

$$\begin{aligned}\tau^t \approx\ & \underbrace{\frac{1}{1-\alpha}\left[\tau^t(\delta) + \left(\frac{\mathrm{d}P}{\mathrm{d}x} + \frac{\mathrm{d}}{\mathrm{d}x}\left(\rho_L\overline{v_L'^2}\right)_{y=\delta}\right)(y-\delta)\right]}_{\text{I }(1)} - \underbrace{\frac{1}{1-\alpha}\int_\delta^{y'}\left\{\frac{\partial}{\partial x}\left[\int_\delta^y(1-\alpha)\rho_L g\,\mathrm{d}y'\right]\right\}\mathrm{d}y}_{\text{II }(\varepsilon)} \\ & + \underbrace{\frac{1}{1-\alpha}\int_\delta^y\left[(1-\alpha)U_L\frac{\partial U_L}{\partial x}\right]\mathrm{d}y}_{\text{III }(\varepsilon)} + \underbrace{\frac{1}{1-\alpha}\int_\delta^y\left[(1-\alpha)V_L\frac{\partial U_L}{\partial y}\right]\mathrm{d}y}_{\text{IV }(\varepsilon)} \\ & - \underbrace{\frac{1}{1-\alpha}\int_\delta^y\frac{\partial}{\partial x}\left[(1-\alpha)\overline{v_L'^2}\right]\mathrm{d}y}_{\text{V }(\varepsilon)} + \underbrace{\frac{1}{1-\alpha}\int_\delta^y\frac{\partial}{\partial x}\left[(1-\alpha)\overline{u_L'^2}\right]\mathrm{d}y}_{\text{VI }(\varepsilon)}.\end{aligned} \tag{A.4}$$

As a consequence of the horizontal geometry, the turbulent shear stress appears to be controlled, to leading order, by the pressure gradient (I). The other terms of (A.4) are of order ε. The buoyancy term (II) contributes to increase the vertical gradient of the turbulent shear stress and thus increases the stress near the wall, but its contribution is of order ε, i.e. smaller than it should be in a vertical flow (order 1). In a horizontal developing bubble layer, the buoyancy term cannot be considered without taking care of the contribution of the mean liquid velocity gradients (III) + (IV) and of the contribution of the longitudinal gradient of the normal turbulent stresses (V) + (VI).

The shear stress is calculated in section c from Eq. (A.4) by using the measured values of α, the values of U_L measured in two-phase flow, the values of $\overline{u_L'^2}$ measured in sections b and c, the values of $\overline{v_L'^2}$ measured in section c and the numerical solution for V_L deduced from the continuity equation and the values of U_L. The results show (Gabillet, 1998) that among the contributions of order ε, the buoyancy (II) is likely to be the only relevant contribution. Indeed, not only are the

contributions of the normal turbulent stresses (V and VI) negligible, but also the two terms (III and IV) balance each other.

Then the following expression can be used to estimate the shear stress inside the bubble layer:

$$(1-\alpha)\tau^{t}(y) \approx \tau^{t}(\delta) + \frac{d}{dx}\left[P + \rho_L \overline{v_L'^2}\right]_{y=\delta}(y-\delta) - \int_{\delta}^{y}\left\{\frac{\partial}{\partial x}\left[\int_{\delta}^{y'}(1-\alpha)\rho_L g\, dy'\right]\right\}dy. \quad (A.5)$$

Since the RMS velocities are the same as in a single-phase flow, at the bubble layer edge, the shear stress can be expressed versus the shear stress τ_0^t that would exist in single-phase flow for the same pressure gradient:

$$(1-\alpha)\tau^{t}(y) - \tau_0^{t}(y) = \rho_L g \int_{\delta}^{y}\left\{\frac{\partial}{\partial x}\left[\int_{\delta}^{y'}\alpha\, dy''\right]\right\}dy'. \quad (A.6)$$

References

Biesheuvel, A., van Wijngaarden, J., 1984. Two-phase flow equations for a dilute dispersion of gas bubbles in liquid. J. Fluid Mech. 148, 301–318.

Cartelier, A., 1990. Optical probes for local void fraction measurements: characterization of performance. Rev. Sci. Instrum. 61, 874–886.

Clark, N.N., Turton, R., 1988. Chord length distributions related to bubble size distributions in multiphase flows. Int. J. Multiphase Flow 14, 413–424.

Eppinger, K., 1995. Etude du mouvement des bulles dans une turbulence homogène isotrope. Thesis, INP Toulouse, France.

Gabillet, C., 1998. Etude expérimentale d'un écoulement turbulent en canal horizontal avec injection pariétale de bulles. Thesis, Institut National Polytechnique, Toulouse, France.

Gabillet, C., Colin, C., Fabre, J., Larrauri, D., Brière, E., 1998. Experimental study of bubble injection in a turbulent boundary layer. In: Proceedings of the 3rd International Conference on Multiphase Flow, Lyon, France, June 8–12.

Herringe, R.A., Davis, M.R., 1976. Structural development of gas–liquid mixture flows. J. Fluid Mech. 73, 97–123.

Hussain, A.K.M.F., Reynolds, W.C., 1975. Measurements in fully developed turbulent channel flow. J. Fluids Eng., 568–580.

Kamp, A., 1996. Ecoulements turbulents à bulles dans une conduite en micropesanteur. Thesis, Institut National Polytechnique, Toulouse, France.

Kowe, R., Hunt, J.C., Hunt, A., Couet, B., 1988. The effect of bubbles on the volume fluxes and the pressure gradients in unsteady and non-uniform flows in liquids. Int. J. Multiphase Flow 14, 587–606.

Laufer, J., 1951. Investigation of turbulent flow in a two-dimensional channel. Report No. 1053, National Advisory Committee for Aeronautics.

Ligrani, P.M., Moffat, R.J., 1986. Structure of transitionally rough and fully rough turbulent boundary layers. J. Fluid Mech. 162, 69–98.

Liu, T.J., Bankoff, S.G., 1993. Structure of air–water bubbly flow in a vertical pipe – I. Liquid mean velocity and turbulence measurements. Int. J. Heat Mass Transfer 36, 1049–1060.

Madavan, N.K., Deutsch, S., Merkle, C.L., 1984. Reduction of turbulent skin friction by micro-bubbles. Phys. Fluids 27 (2), 356–363.

Madavan, N.K., Deutsch, S., Merkle, C.L., 1985. Measurements of local skin friction in a microbubble-modified turbulent boundary layer. J. Fluid Mech. 156, 237–256.

Marié, J.L., 1987. Modelling of the skin friction and heat transfer in turbulent two-component bubbly flows in pipes. Int. J. Multiphase Flow 13, 309–325.

Marié, J.L., Moursali, E., Tran-Cong, S., 1997. Similarity law and turbulence intensity profiles in a bubbly boundary layer at low void fractions. Int. J. Multiphase Flow 23, 227–247.

Maxworthy, T., Gnann, C., Kürten, M., Durst, F., 1996. Experiments on the rise of air bubbles in clean viscous liquids. J. Fluid Mech. 321, 421–441.

Moursali, E.M., Marié, J.L., Bataille, J., 1995. An upward turbulent bubbly boundary layer along a flat plate. Int. J. Multiphase Flow 21, 107–117.

Nakoryakov, V.E., Kashinski, O.N., 1995. Gas–liquid bubbly flows in a near-wall region. In: Proceedings of the 1st International Symposium on Two-phase Flow Modelling and Experimentation, Rome, Italy, pp. 453–457.

Nakoryakov, V.E., Kashinsky, O.N., Burdukov, A.P., Odnoral, V.P., 1981. Local characteristics of upward gas–liquid flows. Int. J. Multiphase Flow 7, 63–81.

Nakoryakov, V.E., Kashinsky, O.N., Randin, V.V., Timkin, L.S., 1996. Gas–liquid bubbly flow in vertical pipes. J. Fluids Eng. 118, 377–382.

Peebles, F.N., Garber, H.J., 1953. Studies of motion of gas bubbles in liquids. Chem. Eng. Progr. 49, 88–97.

Poorte, R.E.G., 1998. On the motion of bubbles in active grid generated turbulent flows. Ph.D. Thesis, University of Twente, The Netherlands.

Roig, V., 1993. Zone de mélange d'écoulements diphasiques à bulles. Thesis, Institut National Polytechnique, Toulouse, France.

Sato, Y., Sadatomi, M., Sekoguchi, K., 1981. Momentum and heat transfer in two-phase bubble flow – I. Int. J. Multiphase Flow 7, 167–177.

Serizawa, A., Kataoka, I., 1990. Turbulence suppression in bubbly two-phase flow. Nucl. Eng. Des. 122, 1–16.

Serizawa, A., Kataoka, I., Michiyoshi, I., 1975. Turbulence structure of air–water bubbly flow – I. Measuring techniques. Int. J. Multiphase Flow 2, 221–233.

Spelt, P.D.M., Biesheuvel, A., 1997. On the motion of gas bubbles in homogeneous isotropic turbulence. J. Fluid Mech. 336, 221–244.

Tjiptahardja, T., Gabillet, C., Colin, C., Boree, J., Fabre, J., 1996. LDA investigation of a turbulent liquid flow with air blowing at a wall. In: 8th International Symposium on Applications of Laser Techniques to Fluid Mechanics, Lisbon, Portugal, July 8–11.

Velidandla, V., Putta, S., Roy, R.P., Kaira, S.P., 1995. Velocity field in turbulent subcooled boiling flow. ASME I: J. Heat Transfer 12, 107–123.

Wang, S.K.L., 1985. Three dimensional turbulence structure measurements in air–water two-phase flow. Ph.D. Thesis, Rensselaer Polytechnic Institute, Troy, NY, USA.

Zun, I., 1988. Transition from wall void peaking to core void peaking in turbulent bubbly flow. In: Afgan, N.H. (Ed.), Transient Phenomena in Multiphase Flow, ICHMT International Seminar. Hemisphere, Washington, pp. 225–245.